

Towards the phase diagram of fermions coupled with $SO(3)$ quantum links in $(2 + 1) - D$

Graham Van Goffrier,^{a,*} Debasish Banerjee,^b Bipasha Chakraborty,^a Emilie Huffman^c and Sandip Maiti^b

^aDepartment of Physics and Astronomy, University of Southampton,
University Road, Southampton SO17 1BJ, UK

^bTheory Division, Saha Institute of Nuclear Physics, 1/AF Bidhannagar, Kolkata 700064, India

^bHomi Bhabha National Institute, Training School Complex, Anushaktinagar, Mumbai 400094, India

^cPerimeter Institute for Theoretical Physics,
31 Caroline St N, Waterloo, ON N2L 2Y5, Canada

E-mail: gwvg1e23@soton.ac.uk, debasish.banerjee@saha.ac.in,
b.chakraborty@soton.ac.uk, ehuffman@perimeterinstitute.ca,
sandip.maiti@saha.ac.in

Quantum link models (QLMs) are generalizations of Wilson's lattice gauge theory formulated with finite-dimensional link Hilbert spaces. In certain cases, the non-Abelian Gauss Law constraint can be exactly solved, and the gauge invariant subspace embedded onto local spin Hamiltonians for efficient quantum simulation. In $(1 + 1)d$ previous studies of the $SO(3)$ QLM coupled to adjoint fermionic matter have been shown to reflect key properties of QCD and nuclear physics, including distinct confining/deconfining phases and hadronic bound states. We extend the model to $(2 + 1)d$ dimensions for the first time, and report on our initial results. We review the construction of gauge-invariant state space for the proposed models, and study the single-plaquette ground state via exact-diagonalisation. We provide indications of a rich phase diagram which shows both spontaneous and explicit chiral symmetry breaking, confinement, and distinct magnetic phases characterised by different plaquette expectation values.

The 41st International Symposium on Lattice Field Theory (Lattice 2024)
July 28th - August 3rd, 2024
University of Liverpool, Liverpool, UK

*Speaker

1. Introduction

Lattice gauge theories (LGTs) have proven in recent decades to be an indispensable tool for extracting quantitative predictions from the Standard Model, especially non-perturbative contributions stemming from quantum chromodynamics (QCD). In combination with renormalized perturbative calculations, lattice QCD (LQCD) has allowed numerous measured observables to be compared with high-quality theoretical values.

As a computational framework, LQCD has typically relied upon the Monte Carlo sampling of path-integral formulated in Euclidean time, to avoid the sign problem. While static, ground state, and thermodynamic properties can be computed very well in this approach, studies of real-time QCD dynamics and properties of QCD matter at finite baryon density suffer from a severe sign problem. It is widely hoped [1] that quantum computation may allow for the simulation of LQCD and other many-body quantum systems in the long-term without exponentially-scaling resources.

In this work we turn to quantum link models (QLMs) [2] as a framework that is especially suited to quantum computation approaches. In contrast to the Wilsonian formulation, the quantum link formulation provides an additional parameter: the representation of link operators, which controls the Hilbert space of local gauge fields and has an exact local gauge invariance. Each such choice of representation leads to a valid theory in its own right with that same gauge invariance. There is thus no need for a gauge-symmetry breaking truncation of the infinite-dimensional Hilbert space needed for each gauge link in the Wilson gauge formulation. QLMs have been studied with increasing interest by several groups, including through classical simulations employing exact-diagonalisation (ED) and tensor networks (TN) [3–5], and on real quantum hardware [6–8]. Most often, Abelian $U(1)$ QLMs have been investigated, with and without matter, but only a few results exist for the physics of $SU(2)$ and $SO(3)$ gauge theories [9–11].

We choose to focus on the $SO(3)$ QLM because of qualitative properties it is known to share with QCD, including fermionic baryon bound states, and spontaneous chiral symmetry breaking (in $(1 + 1)d$). Refs. [9] and [10] were the first to demonstrate these properties with numerical simulations in $(1 + 1)d$, including with dynamical matter fermions. More recently, a subset of us [11] have studied the matter-free $SO(3)$ QLM in $(2 + 1)d$ using quantum algorithms to demonstrate the spontaneous symmetry breaking in that theory.

Here we present the first ED results obtained for the $SO(3)$ QLM in $(2 + 1)d$ including dynamical matter fermions, and show that even on a single plaquette, the model demonstrates both explicit and spontaneous chiral symmetry breaking, as well as other intriguing properties such as distinct magnetic phases. In Section 2, we define the $SO(3)$ QLM and show how to solve the Gauss's Law constraint in $(2 + 1)d$, arriving at a fully gauge-invariant Hilbert space. In Section 3 we overview our ED techniques and the symmetry-driven speedups which enable such a study, and in Section 4 we deliver our numerical results, before discussing implications and continuing work in Section 5.

2. $SO(3)$ Quantum Link Models with Fermions

QLMs succeed in exactly preserving local gauge invariance by modifying the commutation relations between the quantum link fields, which do not affect the gauge invariance. Consequently,

the operators are not unitary. Explicit representations of the link operators and their canonical momenta (the electric fields) can be obtained via an appropriate embedding algebra. Following the notation of [10], we review here the gauge and fermion operators of our construction, implement the $so(6)$ embedding algebra, and then solve Gauss's Law.

2.1 Operators and Gauge-Invariant States

The complete $SO(3)$ operator algebra on each site is:

$$\begin{aligned} [L^a, L^b] &= 2i\varepsilon^{abc} L^c, \quad [R^a, R^b] = 2i\varepsilon^{abc} R^c, \\ [L^a, O^{bd}] &= 2i\varepsilon^{abc} O^{cd}, \quad [R^a, R^{bd}] = -2i\varepsilon^{abc} O^{cd}, \\ [O^{ab}, O^{cd}] &= 2i\delta^{ac} \varepsilon^{abd} R^e + 2i\delta^{bd} \varepsilon^{eac} L^e, \end{aligned} \quad (1)$$

where L^a , R^a and O^{ab} are the $SO(3)$ matrix-valued left/right electric fields and gauge fields, respectively, with colour indices $a, b \in 1, 2, 3$ while spacetime labels are suppressed. We include staggered fermionic matter fields ψ^a which transform in the adjoint representation of $SO(3)$. This has the important consequence that the colour of the fermion can be screened by the colour of a gauge field in order to form a hadronic state, which can be fermionic in nature, as in QCD. In contrast, while considering matter in the fundamental representation, one only obtains bosonic hadronic states.

The generators of gauge transformations at each site may then be written [10]:

$$G^a = -2i\psi^{b\dagger} \varepsilon^{abc} \psi^c + \sum_k \left(L_{x,+k}^a + R_{x,-k}^a \right), \quad (2)$$

such that gauge-invariant states must satisfy $G^a |\Psi\rangle = 0$; this is Gauss's Law. It is also standard practice to encode the above operator algebra by means of an $so(6)$ embedding algebra composed of spin bilinears:

$$O_{x,x+k}^{ab} = \sigma_{x,+k}^a \otimes \sigma_{x+k,-k}^b, \quad L_{x,+k}^a = \sigma_{x,+k}^a \otimes \mathbb{I}, \quad R_{x,-k}^a = \mathbb{I} \otimes \sigma_{x,-k}^a. \quad (3)$$

When we write down gauge-field states, we can then use the notation $|\uparrow\rangle, |\downarrow\rangle$ for spin states, as well as the convention $S^a = \frac{1}{2}\sigma^a$ for spin operators.

Schematically, each $|\Psi\rangle$ at a site is a product of gauge-field and fermion states, i.e. $|\Psi\rangle = |\chi\rangle_g |\psi\rangle_f$, where on a $(2 + 1)d$ square lattice $|\chi\rangle_g$ will receive contributions from four links. A gauge-invariant singlet $|\Psi\rangle$ may therefore be built either from both singlet gauge and fermion components, or from ‘‘matching’’ triplet gauge and fermion components.

The former case is more trivial. $|\psi\rangle_f$ will be a gauge-invariant singlet only in the case of fermionic zero occupation $|0\rangle_f$ or maximum occupation $|3\rangle_f$. As shown in [10], there are two pure-gauge singlets in $(2 + 1)d$, which we denote $|\chi_1\rangle_g$ and $|\chi_2\rangle_g$. Taking all products of these, we have identified four singlet-singlet gauge-invariant states:

$$\begin{aligned} |\Psi_1\rangle &= |\chi_1\rangle_g |0\rangle_f, \quad |\Psi_2\rangle = |\chi_2\rangle_g |0\rangle_f, \quad |\Psi_9\rangle = |\chi_1\rangle_g |3\rangle_f, \quad |\Psi_{10}\rangle = |\chi_2\rangle_g |3\rangle_f, \\ |\chi_1\rangle_g &= \frac{1}{2} (|\uparrow\uparrow\uparrow\downarrow\rangle - |\uparrow\downarrow\downarrow\uparrow\rangle - |\downarrow\uparrow\uparrow\downarrow\rangle + |\downarrow\downarrow\downarrow\uparrow\rangle), \\ |\chi_2\rangle_g &= \frac{1}{\sqrt{12}} (2|\uparrow\uparrow\uparrow\downarrow\rangle + 2|\downarrow\downarrow\downarrow\uparrow\rangle - |\uparrow\downarrow\uparrow\downarrow\rangle - |\uparrow\downarrow\downarrow\uparrow\rangle - |\downarrow\uparrow\uparrow\downarrow\rangle - |\downarrow\downarrow\downarrow\uparrow\rangle), \end{aligned} \quad (4)$$

where the spin (gauge-field) basis is ordered around the vertex, e.g. clockwise.

The latter case requires more construction. Pure-gauge triplet states may be obtained by constructing products of a singlet spin-pair on two links and a triplet spin-pair on the other two links [9], and then applying spin-raising operators. Nine independent states result, denoted as $\{|\chi_3\rangle_g, \dots, |\chi_{11}\rangle_g\}$. These may be combined with single-occupation fermion states $|1\rangle_f$ via the ansatz:

$$|\Psi\rangle = \left[\frac{1}{2}(S^- |\chi_{S_z=0}\rangle_g - S^+ |\chi_{S_z=0}\rangle_g)\psi^{1\dagger} + \frac{i}{2}(S^- |\chi_{S_z=0}\rangle_g + S^+ |\chi_{S_z=0}\rangle_g)\psi^{2\dagger} + |\chi_{S_z=0}\rangle_g \psi^{3\dagger} \right] |0\rangle_f \quad (5)$$

where $|\chi_{S_z=0}\rangle_g$ may be any of $|\chi_6\rangle_g, |\chi_7\rangle_g, |\chi_8\rangle_g$. This ansatz satisfies $G^a |\Psi\rangle = 0$, as does the obvious generalisation to double-occupation fermion states. Therefore, we have identified six triplet-triplet gauge-invariant states, for a total dimensionality of ten gauge-invariant states per site.

2.2 Action of Gauge-Invariant Operators

The only gauge-invariant operators for the above state space are composed of either two fermion-operators, two gauge-operators, or one of each:

$$\begin{aligned} M &= \sum_{a=1}^3 \psi^{a\dagger} \psi^a, & \Phi_{ij} &= \sum_{a=1}^3 S_i^a S_j^a \\ B_i^+ &= \sum_{a=1}^3 2\psi^{a\dagger} S_i^a, & B_i^- &= \sum_{a=1}^3 2\psi^a S_i^a \end{aligned} \quad (6)$$

Applying these operators to the gauge-invariant basis defined above, we arrive at matrix representations convenient for ED, which are illustrated in Figure 1. M is easily seen to count fermion occupation number, while B_i^\pm are generalised raising/lowering operators which mix the gauge degrees of freedom, and the Φ_{ij} are purely gauge-mixing.

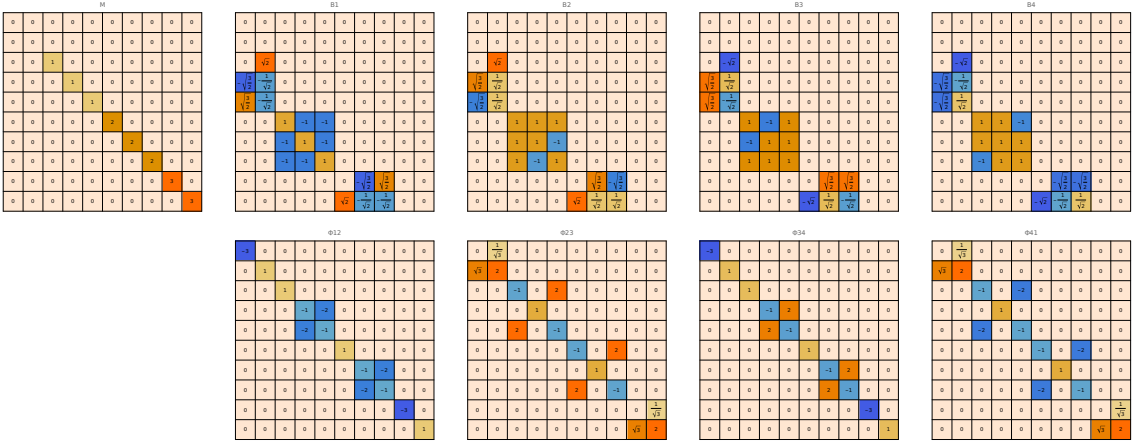


Figure 1: Gauge-invariant operators acting at each site, written in the $|\chi_i\rangle$ basis.

As shown in [10], the Hamiltonian can be re-expressed in terms of these operators, effectively pre-diagonalising it in the gauge-invariant subspace:

$$H = -t \sum_{x, \hat{k}} \left[s_{x, x+\hat{k}} \vec{B}_{x, \hat{k}}^+ \cdot \vec{B}_{x+\hat{k}, -\hat{k}}^- + \text{h.c.} \right] + m \sum_x s_x M_x - \frac{1}{4g^2} \sum_x \text{Tr} [\Phi_{12} \Phi_{41} \Phi_{34} \Phi_{23}] + G \sum_x M_x^2 + V \sum_{x, \hat{k}} M_x M_{x+\hat{k}}, \quad (7)$$

where $s_x = (-1)^{x_1+x_2}$ and $s_{x, \hat{k}} = (-1)^{x_1+\dots+x_{k-1}}$ are alternating signs, spacetime indices on the Φ operators follow a counterclockwise plaquette ordering, and the correspondence between axes \hat{k} and indices $i \in \{1, 2, 3, 4\}$ is most easily understood from the schematic in Figure 2.

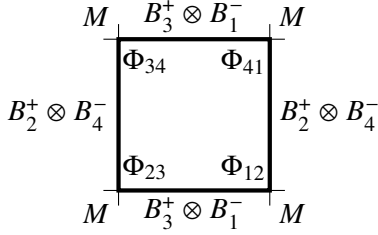


Figure 2: Operator schematic for a single-plaquette lattice.

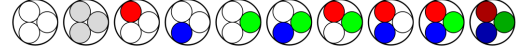


Figure 3: Symbolic notation for 10 gauge-invariant states per site.

3. Exact Diagonalisation Methodology

We perform ED by explicitly constructing the Hamiltonian as a sparse matrix whose entries are simple rational functions of the physical parameters $\{t, m, g, G, V\}$, then substituting chosen values when runs are performed. Each run consists of a Lanczos (Arnoldi) iteration procedure to prepare the ground state of the Hamiltonian [12]. Both sparse matrix storage/retrieval and Lanczos iteration are accelerated by pre-diagonalising the Hamiltonian with respect to its global baryon-number symmetry:

$$B = \sum_x \left(M_x - \frac{3}{2} \mathbb{I}_{10} \right), \quad [B, H] = 0. \quad (8)$$

Labelling global fermion states of the lattice by a row-major ordering of occupation numbers at each site, e.g. $|\Psi_9\rangle \otimes |\Psi_3\rangle \otimes |\Psi_8\rangle \otimes |\Psi_1\rangle \equiv |3120\rangle$, we observe that the eigenvalue of B on a basis state is simply the sum of these occupation numbers less $3N/2$, where N is the total number of sites. Therefore, the $B = 0$ sector corresponds to all N -part partitions (allowing 0) of $3N/2$, which can be easily computed for small N . For the single-plaquette $N = 4$, there are 44 such states, which expand to 1878 states once gauge degrees of freedom are accounted for, out of 10^4 total physical states.

Although the baryon number of the ground state is not 0 for all choices of parameters $\{t, m, g, G, V\}$, and we have analytically understood its variation with the Fermi couplings G, V in particular, we restrict ourselves to the $B = 0$ sector for the analysis presented here. In the continuum limit, the ground state of $SO(3)$ gauge theory is expected to be $B = 0$ across all accessible physical parameters, where the baryon number symmetry is not broken spontaneously.

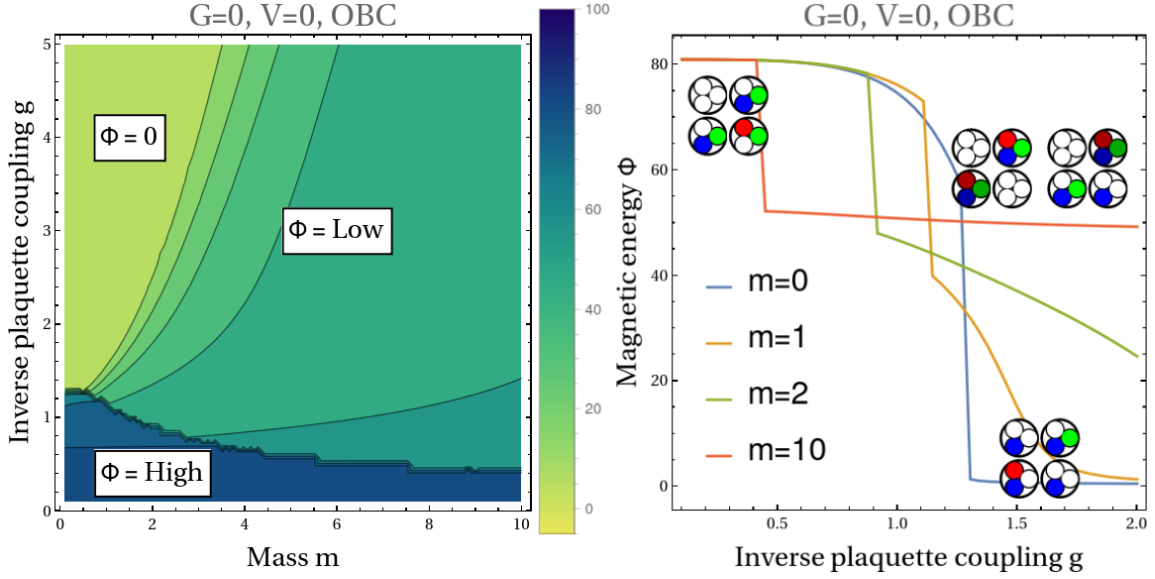


Figure 4: Ground-state plaquette observable $\langle\Phi\rangle$ for varied fermion mass m and inverse plaquette coupling g .

4. Chiral and Magnetic Observables for a Single Plaquette

A standard gauge-invariant observable in LQCD is the average spatial plaquette $\langle\Phi\rangle$, or in our notation, the expectation value of $\text{Tr}[\Phi\Phi\Phi\Phi]$. This quantity is known to be a good order parameter for bulk thermodynamics, and can also be interpreted as an average magnetic field energy. For example, in the $(3+1)d$ Z_2 lattice gauge theory, $\langle\Phi\rangle$ exhibits a large discontinuity at the first-order phase transition [13, 14].

Even for a single plaquette, we can expect that $\langle\Phi\rangle$ may behave quite differently at strong- and weak-coupling, and in response to four-Fermi couplings. Notably, this observable is sensitive to both gauge and fermionic degrees of freedom, and is trivially absent from the $(1+1)d$ physics of [10].

Let us first put the four-Fermi couplings to the side, and observe via ED on a single-plaquette how $\langle\Phi\rangle$ varies just with inverse plaquette coupling g and fermion mass m . The contour plot in Figure 4 (left) reveals three distinct phases: $\langle\Phi\rangle \sim 0$ (zero-field), $\langle\Phi\rangle \sim 50$ (low), and $\langle\Phi\rangle \sim 80$ (high). The high-field region occurs only at stronger plaquette couplings (smaller g), with the critical coupling g_C between zero-field and high-field regions especially sharp in the massless limit. As illustrated in 4 (right), the high-field region becomes narrower for nonzero fermion mass m . Meanwhile, at weaker plaquette couplings g , the introduction of mass gradually transitions zero-field behavior to low-field behavior. We also remark that increased $\langle\Phi\rangle$ is associated with a confining of fermions, as denoted by state schematics in the Figure – the high-field behavior is associated with a cluster of fermion occupation towards one corner of the plaquette, while the low-field behavior is associated with checkerboarded zero-occupation and full-occupation sites.

We are also interested in the spontaneous breakdown of chiral symmetry. For the $SO(3)$ QLM, a phase with spontaneously-broken chiral symmetry is signified by a staggered fermion occupation pattern, as well as a diminishing gap between the ground state and first excited state. We can expect

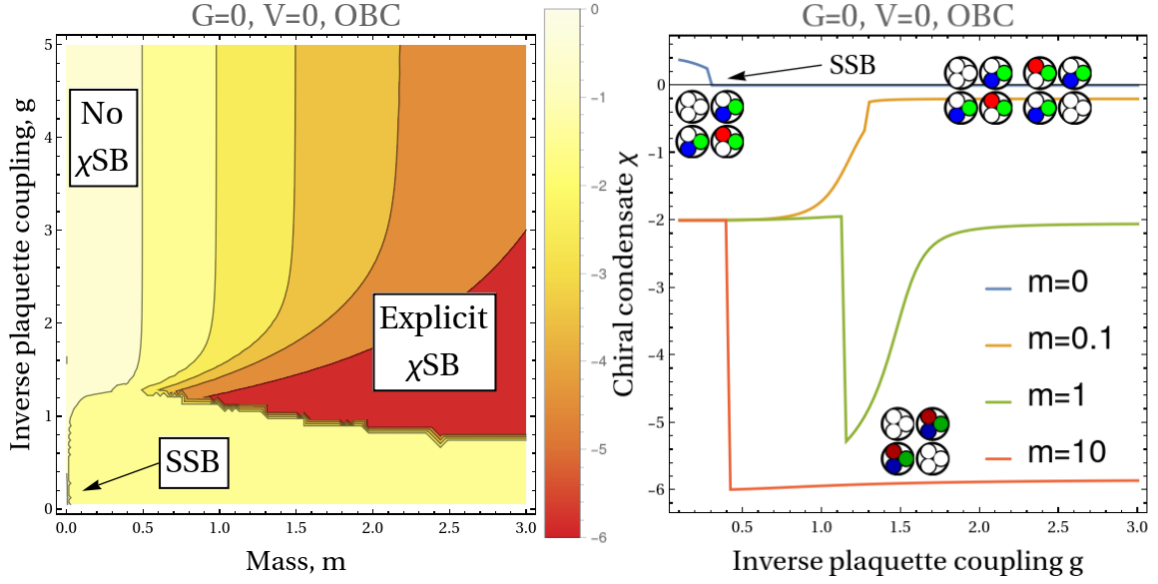


Figure 5: Ground-state chiral condensate observable $\langle \bar{\Psi}\Psi \rangle$ for varied fermion mass m and inverse plaquette coupling g .

a nonzero mass term to explicitly break chiral symmetry. To assess these properties, we examine the chiral condensate observable $\langle \bar{\Psi}\Psi \rangle$, or in our notation, the expectation value of $\sum_x s_x M_x$.

Via our ED on a single-plaquette, we observe how $\langle \bar{\Psi}\Psi \rangle$ varies with inverse plaquette coupling g and fermion mass m . The contour plot in Figure 5 (left) reveals three distinct phases: $\langle \bar{\Psi}\Psi \rangle \sim 0$ (chiral symmetry preserved), $|\langle \bar{\Psi}\Psi \rangle| \sim 6$ (maximal chiral symmetry-breaking), and $|\langle \bar{\Psi}\Psi \rangle| \sim 2$ (weak chiral symmetry-breaking). For nonzero fermion masses, chiral symmetry-breaking is unavoidable, but above about $m \gtrsim 1$ the maximal and weak regions are separated by a sharp transition. This transition notably but imprecisely aligns with the low-field to high-field transition in the plaquette observable, as seen in Figure 4.

At $m = 0$, while chiral symmetry is broadly preserved as could be expected, there is a critical inverse plaquette coupling g_χ below which chiral symmetry is again weakly broken. $g_\chi \neq g_C$, as more cleanly illustrated by comparing chiral condensates for several fixed fermion masses, seen in Figure 5 (right). Even a very small nonzero mass ($m \sim 10^{-7}$) dilutes this effect, returning to an explicitly symmetry-breaking regime. For couplings stronger than g_χ in the massless limit, the mass-gap is also seen to vanish.

We are now in a position to ask how each of these phases is perturbed by the four-Fermi interactions, and choose to focus on the massless case. The dependence of the magnetic critical coupling g_C on G and V is demonstrated in Figure 6, while the same dependence of the spontaneous chiral symmetry-breaking critical coupling g_χ is seen in Figure 7.

The zero-field to high-field transition in the plaquette observable is stable for positive anisotropies G , which energetically penalises sites with extremal fermion occupation (0 or 3). This also aligns with the preliminary observation that positive G shrinks the low-field region. For $G < 0$, however, the zero-field to high-field transition becomes smooth, unless a sufficiently strong nearest-neighbor coupling V is also introduced (numerically, the boundary is $V \sim -2G$). Interestingly, the critical

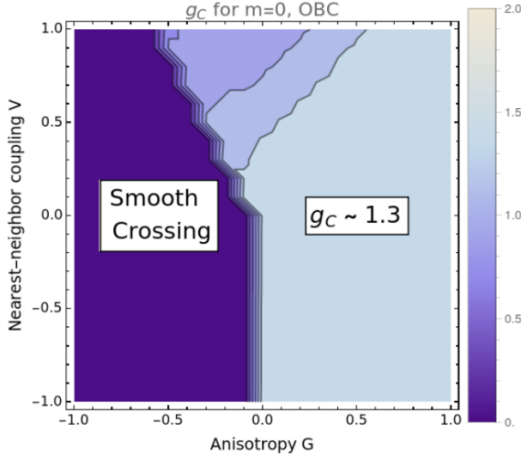


Figure 6: Magnetic critical coupling g_C for massless fermions $m = 0$, as a function of four-fermi couplings G and V . In all cases the model transitions from a zero-field to a high-field regime, but to the left of the obvious boundary line this occurs smoothly, while to the right the critical value slowly retreats with increased V .

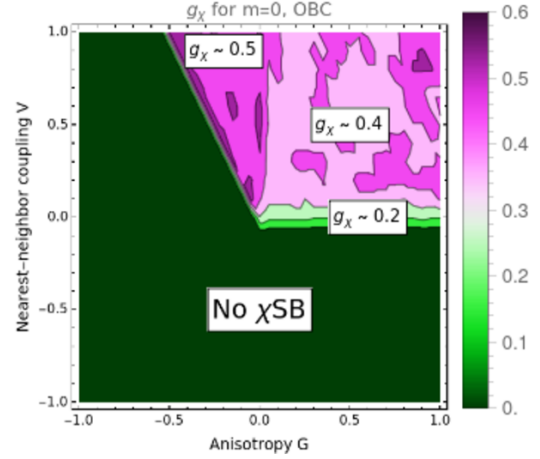


Figure 7: Spontaneous chiral symmetry-breaking critical coupling g_χ for massless fermions $m = 0$, as a function of four-fermi couplings G and V . To the left and below of the boundary line, the chiral symmetry remains unbroken, and a notably stronger plaquette coupling g is required on the positive G -axis.

inverse plaquette coupling g_C only notably changes as the nearest-neighbor coupling V is increased; it is unclear whether the transition remains discontinuous as $V \rightarrow \infty$, or if a critical endpoint could be identified somewhere on the $V \sim -2G$ line.

We should expect that negative nearest-neighbour coupling V would preclude any chiral symmetry-breaking by favouring “ferromagnetic” states with $\langle \bar{\Psi}\Psi \rangle = 0$. This expectation is confirmed by ED, alongside a similar role of the $V \sim -2G$ diagonal line as for the magnetic observable. The spontaneous chiral symmetry-breaking phenomenon is somewhat stable for $V > 0$ and G to the right of this diagonal. Another notable feature is that the sign of G distinguishes two regions of slightly distinct spontaneous chiral symmetry-breaking critical coupling g_χ .

5. Discussion

While the $SO(3)$ QLM in $(2+1)d$ is an interesting quantum system in its own right, ultimately our goal is to quantum simulate QCD and thereby better understand its non-perturbative features. We should therefore take our preliminary one-plaquette results, first and foremost, as an indicator that non-Abelian QLMs with dynamical fermions are robust discretisations of gauge theories capable of exhibiting the core physics properties of QCD, including across the full phase diagram for temperature and baryo-chemical potential.

Adapting and developing quantum algorithms well-suited to simulating QLMs is an essential continuing effort, and to that end we are in the process of constructing quantum circuits to reproduce out ED results on small lattices. Because of the limited availability and reliability of quantum hardware, we are also employing large-scale classical simulations (including ED and matrix product states), to check the stability of the single-plaquette phase diagram as the continuum is approached.

References

- [1] Uwe-Jens Wiese. Towards quantum simulating qcd. *Nuclear Physics A*, 931:246–256, 2014.
- [2] Uwe-Jens Wiese. From quantum link models to d-theory: a resource efficient framework for the quantum simulation and computation of gauge theories. *Philosophical Transactions of the Royal Society A*, 380(2216):20210068, 2022.
- [3] Jad C Halimeh, Maarten Van Damme, Torsten V Zache, Debasish Banerjee, and Philipp Hauke. Achieving the quantum field theory limit in far-from-equilibrium quantum link models. *Quantum*, 6:878, 2022.
- [4] Torsten V Zache, Maarten Van Damme, Jad C Halimeh, Philipp Hauke, and Debasish Banerjee. Toward the continuum limit of a $(1 + 1)$ d quantum link schwinger model. *Physical Review D*, 106(9):L091502, 2022.
- [5] Yi-Ping Huang, Debasish Banerjee, and Markus Heyl. Dynamical quantum phase transitions in $u(1)$ quantum link models. *Physical Review Letters*, 122(25):250401, 2019.
- [6] Emilie Huffman, Miguel García Vera, and Debasish Banerjee. Toward the real-time evolution of gauge-invariant z_2 and $u(1)$ quantum link models on noisy intermediate-scale quantum hardware with error mitigation. *Physical Review D*, 106(9):094502, 2022.
- [7] D Banerjee, S Caspar, F-J Jiang, J-H Peng, and U-J Wiese. Nematic confined phases in the $u(1)$ quantum link model on a triangular lattice: Near-term quantum computations of string dynamics on a chip. *Physical Review Research*, 4(2):023176, 2022.
- [8] Jesse Osborne, Bing Yang, Ian P McCulloch, Philipp Hauke, and Jad C Halimeh. Spin- s $u(1)$ quantum link models with dynamical matter on a quantum simulator. *arXiv preprint arXiv:2305.06368*.
- [9] Michael Bögli. *Non-Trivial θ -Vacuum Effects in the 2-d $O(3)$ Model and Quantum Simulation of Non-Abelian Lattice Gauge Theories*. PhD thesis, Universität Bern, 2014.
- [10] Enrique Rico, Marcello Dalmonte, Peter Zoller, Debarghya Banerjee, Michael Bögli, Pascal Stebler, and U-J Wiese. $SO(3)$ “nuclear physics” with ultracold gases. *Annals of physics*, 393:466–483, 2018.
- [11] Sandip Maiti, Debasish Banerjee, Bipasha Chakraborty, and Emilie Huffman. Spontaneous symmetry breaking in a $so(3)$ non-abelian lattice gauge theory in $2 + 1$ d with quantum algorithms. *arXiv preprint arXiv:2409.07108*, 2024.
- [12] Cornelius Lanczos. An iteration method for the solution of the eigenvalue problem of linear differential and integral operators. 1950.
- [13] Michael Creutz. Phase diagrams for coupled spin-gauge systems. *Physical Review D*, 21(4):1006, 1980.
- [14] Michael Creutz and Masanori Okawa. Generalized actions in z_2 lattice gauge theory. *Nuclear Physics B*, 220(2):149–166, 1983.